Applied Catalysis B: Environmental 259 (2019) 118059

Contents lists available at ScienceDirect

Applied Catalysis B: Environmental

journal homepage: www.elsevier.com/locate/apcatb

Nickel catalysts supported on palygorskite for transformation of waste cooking oils into green diesel

Sotiris Lycourghiotis[a,b,d], Eleana Kordouli[c,d], Labrini Sygellou[d], Kyriakos Bourikas[a,*], Christos Kordulis[c,d]

[a] School of Science and Technology, Hellenic Open University, Tsamadou 13-15, GR-26222, Patras, Greece
[b] Department of Civil Engineering, Technological Educational Institute of Western Greece, 1 M. Alexandrou Str., GR-26334, Patras, Greece
[c] Department of Chemistry, University of Patras, GR-26504, Patras, Greece
[d] Foundation of Research and Technology-Institute of Chemical Engineering Science (FORTH/ICE-HT), Stadiou Str. Platani, P.O. Box 1414, GR-26500, Patras, Greece

ARTICLE INFO

Keywords:
Palygorskite
Green diesel
Waste cooking oils
Nickel catalysts
Second
Generation biofuels

ABSTRACT

Nickel catalysts supported on palygorskite of varying Ni content were synthesized following the deposition–precipitation method. The catalysts were characterized using various techniques and evaluated in a semi-batch reactor for the transformation of *waste cooking oils* (WCO) into *green diesel* at 310 °C and hydrogen pressure 40 bar.

The nickel nanoparticles supported on palygorskite were proved to be very active. The conversion of the WCO was about 100%. The green diesel content of the liquid product depends mainly on the nickel surface exposed per gram of catalyst, following a volcano like trend and maximized (81.9 wt %) over the sample with 30 wt % Ni. Taking into account the very high ratio of WCO volume to catalyst mass (100 mL/g) and that the evaluation of the catalysts was performed under solvent free conditions, these results demonstrate the successful use of mineral palygorskite for developing promising "natural catalysts" for green diesel production.

1. Introduction

The production of the "second generation biofuels" does not compete with the production of foods for land and water. Therefore, these are perceived as being more sustainable than the first generation ones (bioethanol, biobutanol and biodiesel) produced from sugars, starches and vegetable oils [1,2]. Two types of biomass can be utilized for the production of the second generation biofuels. First the lignocellulosic biomass of plant waste products, which consists of 40–50% cellulose, 25–35% hemi-cellulose, 15–20% lignin and small amounts of other components [3]. Various biofuels could be potentially produced following different routes. Although the production of biofuels from the lignocellulosic biomass is the subject of intensive research, many scientific and technological problems, related to its complex structure, must be confronted before biofuels may be produced via cost effective processes [4].

The second type of biomass that can be utilized for producing second generation biofuels is the waste cooking oils [5–9], waste animal fat [10,11], distilled fatty acids being in the side stream of the plant oil industries [12,13] and recently oil extracted from spent coffee grounds [14]. This type of biomass is constituted mainly from triglycerides (namely tri-esters of glycerol with fatty acids) and free fatty acids. Therefore, it is much less complex and contains much less oxygen than e.g. bio–oils produced from lignocellulosic biomass. Thus, it seems to be very attractive for producing second generation liquid biofuels. From this type of biomass one may produce n-alkanes with 12–18 carbon atoms (n-C12 – n-C18), namely hydrocarbons in the range of diesel (*green diesel*). This is obtained through selective deoxygenation (SDO) of the natural triglycerides and free fatty acids realized by hydrotreatment under high hydrogen pressure (10–80 bar) and temperatures in the range 260–360 °C. The subject has gained much interest in the last fifteen years [15–18] but in the most of cases natural triglycerides drawn from *vegetable plant oils* and corresponding probe molecules (e.g. free fatty acids, methyl esters of fatty acids) have been used as feedstock [19–23].

Concerning the catalysts that can be used for the transformation of natural triglycerides and free fatty acids to green diesel via the "stand alone approach" [15,24] the research interest is mainly concentrated on the "non-sulphided nickel based catalysts" [25]. The subject was thoroughly reviewed by us in 2016 [16]. Very recent studies on nickel–alumina catalysts reported by our group [26–28] have indicated that quite high nickel content (e.g. 60 wt %) is necessary in order to obtain

* Corresponding author.
E-mail address: bourikas@eap.gr (K. Bourikas).

https://doi.org/10.1016/j.apcatb.2019.118059
Received 18 February 2019; Received in revised form 1 August 2019; Accepted 4 August 2019
Available online 09 August 2019
0926-3373/ © 2019 Elsevier B.V. All rights reserved.

very high active surface and thus high activity. This high active surface was obtained following co-precipitation with a severe control of the precipitation parameters [26,28]. Again, in the great majority of the studies concerning the "non-sulphided nickel based catalysts" *fresh plant oils* were used as feed stock. Studies using waste cooking oils, waste animal fats, distilled fatty acids and oil extracted from spent coffee grounds are very scarce [e.g. 5,6,7,8,9,10,11,12,13,14]. Moreover, the catalysts used so far *are fully synthetic* as it concerns both the support and the supported phase. On the other hand, the exploitation of minerals as "natural" catalytic supports for the development of green diesel production catalysts is very important in the context of sustainable development and the cyclic economy. It is clear that as fossil fuels are exhausted and the need for biofuel production will become more and more imperative, more and more large amounts of catalysts will be needed to speed up the processes involved. Thus, the development of heterogeneous catalysts based on cheap minerals is expected decreasing considerably the cost of catalysts. In spite of the above, efforts utilizing minerals for synthesizing supported nickel catalysts for green diesel production have not been reported so far.

In the present work we are trying to change this situation by developing nickel catalysts supported on "palygorskite", a natural mineral, for the transformation of waste cooking oils (WCO) into green diesel.

Palygorskite is a very attractive cheap mineral that is found in large quantities in different parts of the world. For example, its stocks in our country (Greece) are about 6×10^6 tons. The theoretical molecular formula of the palygorskite is $[Si_8Mg_5O_{20}(OH)_2](H_2O)_4 \times 4H_2O$. However, its chemical composition is differentiated within some limits, depending on the deposit. Typically, Mg^{2+} undergoes isomorphous substitution by Al^{3+} ions (and in lower extent by some other cations). Thus, a more realistic molecular formula would be $[Si_8(Mg_{5-2x}Al_{2x})O_{20}(OH)_2](H_2O)_4 \times 4H_2O$. It consists of two tetrahedral layers of silicate units $[SiO_4]$ containing a layer of octahedral units of Al^{3+} $[AlO_6]$ and Mg^{2+} $[MgO_6]$. Between the so formed triple layers, void spaces are developed in the range of 1–2 nm, creating an open structure. Adsorbed water molecules are located inside these void spaces. Moreover, hydroxyl groups (OH) and protonated hydroxyl groups (OH_2) are bonded to a number of cations.

With regard to the production of nickel catalysts based on palygorskite, the effort seems to concentrate on the development of catalysts for the catalytic cracking of tar produced as by-product in the gasification of the biomass of various plant materials [29–31], as well as for the catalytic cracking of benzene [32], toluene [31,33] or naphthalene [31] used as standard compounds for the tar resulting from the gasification of the biomass in the context of the production of hydrogen or synthesis gas. Finally, in some cases nickel-based catalysts have been developed for steam reforming leading to hydrogen production [e.g. 34]. The present work is a part of the overall effort done in our laboratory to use minerals as catalysts or supports of catalysts for the production of biofuels or other green products [35,36].

2. Experimental

2.1. Preparation of the catalysts

2.1.1. Cleaning palygorskite

The raw material, of Greek origin, was obtained from the Geology Department of the University of Patras (Greece). The original mineral was pulverized in an agate mortar. Then the standard clay fraction method was used for removing the contaminants [37].

2.1.2. Synthesis of the catalysts

The catalysts were prepared by *deposition–precipitation*. In a typical synthesis, a suitable amount of nickel nitrate hexahydrate ($Ni(NO_3)_2.6H_2O$, + 96%, Chem-LabNV) was dissolved in 50 mL water in a spherical flask and then a weighted amount of palygorskite was suspended. Urea (Duchefa) aqueous solution (50 mL) was added, containing the triple amount of urea molecules with respect to the NO_3^- ions of the nickel salt. A reflux condenser and a magnetic stirrer were installed. The spherical flask was immersed in a heated oil bath (110 °C). The suspension remained at 110 °C for 10 h. Then it was cooled down to ambient temperature and filtered. The solid obtained was washed with triply distilled water and dried at 110 °C overnight.

2.1.3. Activation of the catalysts

The hydroxides in the dried samples, formed upon deposition –precipitation, were decomposed in the first step of the activation procedure by increasing temperature (5 °C/min) from room temperature up to 400 °C and then remained at this temperature for 1 h in a stream of Ar (30 mL/ min). This procedure leads to the formation of the *catalyst precursors*. The *catalysts* were obtained by reduction of the catalyst precursors at 500 °C for 2.5 h in a stream of H_2 (30 mL/min). A fixed bed quartz reactor has been used in both activation steps.

2.1.4. Catalysts prepared

Seven catalysts were prepared with different nickel content in the range 0–60 wt % Ni using the aforementioned methodology. The samples were symbolized by 0Ni/MP, 10Ni/MP, 20Ni/MP, 30Ni/MP, 40Ni/MP, 50Ni/MP and 60Ni/MP. The numbers denote the percentage composition (nominal) in nickel (wt %) whereas the symbol (MP) stands for the mineral palygorskite used.

2.2. Characterization of the catalysts

The characterization presented below concerns the reduced catalysts, namely the catalysts after activation. The only exception concerns "temperature programmed reduction" performed on the oxide precursors. The reduced catalysts were again reduced in situ before the x-ray photoelectron measurements (see below).

2.2.1. Spectroscopic determination of the composition

The percentage composition in nickel was determined by spectroscopic determination of the nickel concentration in the solution used for the synthesis of the catalysts and in the solution obtained after filtration [38]. More precisely, dimethylglyoxime (DMG) was added to the solutions and a soluble anionic complex with the formula $Ni(DMG)_2^{2-}$ was obtained. Its concentration was determined at 445 nm. A UV–Vis spectrophotometer (Varian Cary 3) was used for these measurements.

2.2.2. Determination of the porous structure

The BET specific surface area, S_{BET}, the microporous specific surface area, S_{MCR}, the mesoporous–small macroporous specific surface area, S_{BJH}, as well as the mesoporous–small macroporous specific pore volume, V_{BJH}, and the mesoporous–small macroporous pore volume distributions of the catalysts were determined using N_2 adsorption–desorption isotherms recorded using a Micromeritics apparatus (Tristar 3000 porosimeter) and suitable software.

2.2.3. Scanning Electron microscopy - energy dispersive spectrometry (SEM-EDS)

The percentage composition in nickel of the catalysts was also determined by EDS. A Scanning Electron Microscope (SEMJEOL JSM6300) equipped with an Energy Dispersive Spectrometry accessory has been used. The chemical composition of the samples was determined using natural and synthetic standards and 20 kV accelerating voltage with 10 nA beam current. Microanalysis was performed on gold coated samples. The sample powders were mounted directly on the sample holder. The morphology of the samples was examined by SEM using the microscope mentioned above.

2.2.4. Transmittance Electron Microscopy (TEM)

The TEM analysis of the catalysts was performed using a JEOL JEM-

2100 system operated at 200 kV (resolution: point 0.23 nm, lattice 0.14 nm). TEM images were recorded using an Erlangshen CCD Camera (Gatan, Model 782 ES500W). The specimens were prepared by dispersion in water and spread onto a carbon-coated copper grid (200 meshes). The statistical analysis of about 800 black spots at TEM images for a given catalyst, corresponding to the supported particles, allowed determining their size distribution. Assuming spherical shape for Ni nanoparticles and taking into account their size distribution in each sample, the nickel surfaces exposed per gram of Ni and per gram of catalyst were calculated.

2.2.5. X-ray diffraction (XRD)

A Brucker D8 Advance diffractometer equipped with a nickel-filtered CuKα (1.5418 Å) radiation source was used for recording the X-ray diffraction patterns and thus investigating the crystal structure of the catalysts. The step size and the time per step were respectively fixed at 0.02° and 0.5 s in the range of $10° \leq 2\theta \leq 80°$.

2.2.6. Fourier transformed – infrared spectroscopy (FT-IR)

The structure of the support was also approached by FT-IR spectroscopy. The FT-IR spectra of the catalysts were recorded using the "Perkin–Elmer Spectrum 100" spectrophotometer and following the well known technique of KBr wafer. Spectra were recorded at 4 cm^{-1} nominal resolution in the range 500-4000 cm^{-1}.

2.2.7. X-ray photoelectron spectroscopy (XPS)

The surface analysis of the catalysts was performed in a UHV chamber ($P < 10^{-9}$ mbar) consisting of a high pressure cell, a preparation and an analysis chamber. The analysis chamber is equipped with a SPECS LHS-10 hemispherical electron analyzer. The XPS measurements were carried out at room temperature using unmonochromatized MgKa radiation, under conditions optimized for maximum signal (constant ΔE mode with pass energy of 97 eV giving a full width at half maximum (FWHM) of 1.7 eV for the $Ag3d_{5/2}$ peak). The analyzed area was an ellipsoid with dimensions 2.5 × 4.5 mm^2. The XPS core level spectra were analyzed using a fitting routine, which allows the decomposition of each spectrum into individual mixed Gaussian-Lorentzian components after a Shirley background subtraction. The samples were in powder form and pressed into pellets, then they were reduced in the high pressure cell (500 °C in H_2 atmosphere for 5 h) and transferred to analysis chamber for XPS in situ measurements. Wide Scans were recorded for all samples, while the core level peaks that were recorded in detail were: Ni2p, Fe2p, Al2p, Mg2s, Si2p, C1s and O1s. Errors in our quantitative data are found in the range of ~10% (peak areas), while the accuracy for BEs assignments is ~0.1 eV.

2.2.8. Temperature programmed reduction (TPR)

A laboratory-constructed equipment was used for conducting the H_2-TPR experiments. Specifically, 20 mg of the *catalyst precursor* (diluted with 30 mg of quartz powder was placed in a quartz reactor and a mixture of hydrogen/argon (H_2/Ar: 5/95 v/v, flow rate 40 mL min^{-1}) was passed through the reactor for 40 min at room temperature. The temperature was then increased to 1000 °C with a constant rate of 10 °C min^{-1}. The decrease of the hydrogen concentration in the gas mixture due to the reduction was detected by a thermal conductivity detector (TCD) (Shimadzu). The reducing gas mixture was dried in a cold trap (−95 °C) before reaching the TCD.

2.2.9. Temperature programmed desorption of ammonia (NH_3-TPD)

The aforementioned laboratory-constructed equipment was also used for conducting the NH_3-TPD experiments and thus estimating the catalysts acidity. 100 mg of the catalyst were placed in the reactor and helium was passed through the reactor (flow rate 30 mL min^{-1}) for 30 min in order to remove any adsorbed species from the catalyst surface. After that, a stream of NH_3 was introduced in the reactor for 30 min at room temperature and then it switched to He to remove the physically adsorbed ammonia. The temperature was then increased linearly up to 600 °C with a rate of 10 °C/min. The amount of the desorbed ammonia was determined by the aforementioned TCD.

2.2.10. Determination of the equilibrium pH of sample/water suspensions

The equilibrium pH of the catalyst/water suspensions was also used for estimating the acidity of the catalysts: 0.02 g of the solid sample was dispersed in 2 mL of distilled water. Stirring was followed to homogenize the suspension. The suspension was then allowed to stand in order to separate the liquid from the solid. After 10 min pH was measured with a pH-meter (Radiometer Copenhagen ABU901 Autoburette) equipped with a combination pH electrode. The measurement in each sample was repeated after half an hour. No significant changes were observed between the two measurements.

2.2.11. Micro-electrophoresis measurements

Microelectrophoretic measurements were performed at 25 °C using a Zetasizer NanoZS, Malvern. Very dilute catalyst/electrolyte suspensions (10 mg/100 mL) were prepared with constant ionic strength, 0.01 M $NaNO_3$. The pH of the suspensions was adjusted by small additions of a 1 M HNO_3 solution.

2.3. Evaluation of the catalysts

Catalysts performance for transformation of waste cooking oil to green diesel by hydrotreatment was evaluated at 310 °C, hydrogen pressure 40 bar and reactant volume to catalyst mass ratio equal to 100 mL / 1 g. A batch reactor (300 mL, Autoclave Engineers) working in a semi-batch mode was used in all cases. One gram of the catalyst and 100 mL of the reactant were added to the reactor. The reactor was purged three times with Argon. Then it was pressurized with H_2 (40 bar). The hydrogen flow rate was adjusted by a flow controller (Brooks 58505S) at 100 mL/min and the speed of stirring at 1000 rpm. The reactor was heated and the temperature was increased, with a temperature rate 10 °C/min, up to 310 °C. The reaction was monitored for a period of 9 h by analyzing, by gas chromatography, liquid samples withdrawn from the reactor every hour. The sample was diluted 20 times with heptane and 1 μL of the dilute sample was injected into the GC. A Shimadzu GC-2010 plus gas chromatograph equipped with a flame ionization detector (FID) and an appropriate column (SUPELCO, MET-Biodiesel, l = 14 m, d = 0.53 mm, tf = 0.16 μm) has been used. The temperature of the injector and the detector were respectively equal to 350 °C and 390 °C. The temperature in the chromatograph oven was changed as follows: 50 °C for 2 min, increase up to 180 °C with a rate 11 °C/min, 180 °C for 2 min, increase up to 230 °C with a rate 7 °C/min, 230 °C for 1 min, increase up to 380 °C with a rate 15 °C/min, 380 °C for 2 min. Standard n-alkanes purchased from the Supelco were used for product identification and calibration. The product was also identified by gas chromatography-mass spectrometry. A Shimadzu GCMS-QP2010 ultra apparatus has been used. The external standard method (heptane) was followed for determining the composition of the sample.

3. Results and discussion

3.1. Catalysts composition

The catalysts composition is given in Table 1. It may be seen that the actual percentage nickel loadings determined by photometrical analysis (PA) and EDS are similar and very close to the corresponding nominal values for the samples 0Ni/MP - 40Ni/MP. Slightly lower values were determined by both techniques in the samples 50Ni/MP and 60Ni/MP. Moreover, the mapping of the nickel obtained by EDS has shown almost uniform nickel distribution at micro-scale. A typical mapping is illustrated in Figure S1. Almost identical relative elemental composition was obtained for the support in all samples taking into account that the

Table 1
Nickel loading (% wt) of catalysts determined by photometrical analysis (PA) and EDS, % atomic composition of the support and the corresponding chemical formula of the support in the catalysts prepared.

Catalyst	Ni (%wt)		% atoms in the support					Chemical formula of palygorskite in the catalysts
	PA	EDS	Si	Fe	Mg	Al	O	
0Ni/MP	–	–	23.96	6.04	9.86	1.11	59.03	$[Si_8Mg_{3.9}Al_{0.4}Fe_{1.2}O_{20}(OH)_2](H_2O)_4 4H_2O$
10Ni/MP	9.96	11.90	21.42	7.39	7.95	0.71	50.07	$[Si_8Mg_{3.4}Al_{0.3}Fe_{1.3}O_{20}(OH)_2](H_2O)_4 4H_2O$
20Ni/MP	19.00	18.53	24.73	5.22	10.4	1.25	39.02	$[Si_8Mg_{3.8}Al_{0.4}Fe_{0.8}O_{20}(OH)_2](H_2O)_4 4H_2O$
30Ni/MP	28.75	30.17	18.39	5.13	5.92	0.55	39.84	$[Si_8Mg_{2.9}Al_{0.25}Fe_{1.2}O_{20}(OH)_2](H_2O)_4 4H_2O$
40Ni/MP	38.50	38.02	18.88	4.26	7.15	0.88	31.91	$[Si_8Mg_{3.5}Al_{0.4}Fe_{0.9}O_{20}(OH)_2](H_2O)_4 4H_2O$
50Ni/MP	47.80	43.61	16.98	3.15	7.91	1.78	28.86	$[Si_8Mg_{4.3}Al_{0.8}Fe_{0.7}O_{20}(OH)_2](H_2O)_4 4H_2O$
60Ni/MP	57.30	55.87	13.66	2.16	5.17	0.89	23.42	$[Si_8Mg_{3.5}Al_{0.5}Fe_{0.9}O_{20}(OH)_2](H_2O)_4 4H_2O$

accuracy of EDS is no better than 10% (Table 1). This indicates that the relative elemental composition of the support was not changed upon its contact with the nitrate and urea aqueous solutions.

3.2. Solid phases

The solid phases formed on the catalysts were investigated by XRD, FT-IR, electron diffraction and XPS. The XRD patterns recorded for the samples are illustrated in Figure S2. The 2θ values of the peaks and their relative intensities obtained for the samples MP and 0Ni/MP correspond to palygorskite (COD 9010432). It may be seen that upon the treatment of the mineral palygorskite for catalysts preparation, it undergoes a significant decrease of its crystallinity. The XRD patterns show moreover, that the deposition of the nickel does not disturb the main crystal structure of palygorskite. This is corroborated by the FT-IR results (Figure S3). According to the literature [39–44] the IR peaks at 674, 796 και 805 cm^{-1} can be attributed to bending vibrations of the Si-O-Si skeletal units of the tetrahedral sheets of palygorskite, whereas the peaks in the range 1000–1200 cm^{-1} to the stretching vibrations of the same units. Moreover, the peaks at 1640 and 3443 cm^{-1} are attributed, respectively, to the bending and stretching vibrations of adsorbed/coordinated water molecules. The deposition of nickel on palygorskite does not change the peak positions of the aforementioned absorption bands confirming the stability of the palygorskite structure deduced by XRD.

Returning to the XRD patterns (Figure S2), we are observing three additional peaks for the samples containing nickel at 2θ: 44.38° [(111) d = 0.200 nm], 51.72° [(200), d = 0.177 nm] and 76.17° [(220), d = 0.126 nm]. These are indicative of supported nickel nanoparticles (JCPDS 04-0850) and are also detected by electron diffraction. Two typical electron diffraction patterns are illustrated in Fig. 1.

The d values 0.200, 0.177 and 0.126 nm corresponding, respectively, to (111), (200) and (220) crystal planes of the supported nickel particles are illustrated. The d = 0.250 nm is attributed to the crystal plane (111) of very small NiO nanocrystals (JCPDS 22-1189) non-detectable by XRD (Fig. S2). The nickel (111) and the NiO (111) crystal planes are also identified in the HRTEM images. A typical example is illustrated in Figure S4.

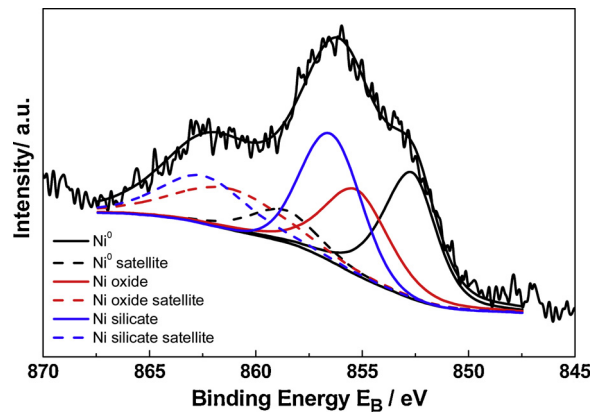

Fig. 2. Deconvoluted $Ni2p_{3/2}$ XP spectrum of the 30Ni/MP catalyst.

The supported solid phases were moreover investigated by XPS. Fig. 2 displays a detailed XP deconvoluted spectrum in the region of $Ni2p_{3/2}$ peaks for the sample 30Ni/MP, taken as an example. The corresponding spectra for all catalysts are illustrated in Figure S5.

Inspection of Fig. 2 reveals that the $Ni2p_{3/2}$ peak is deconvoluted into three components. The peak at binding energy 852.8 ± 0.1 eV with the satellite peak at ~858.0 eV is assigned to Ni^0, indicating the formation of nickel metallic particles, in full agreement with the XRD, electron diffraction and HRTEM results. The peak at 855.2 eV with the satellite peak at ~861.0 eV is assigned to NiO [45], again in agreement with the electron diffraction and HRTEM results. The peak at 856.4 ± 0.1 eV with the satellite peak at ~862.5 eV is assigned to nickel silicate hydroxide $[Ni_3Si_2O_5(OH)_4]$ [46] and/or to nickel silicate $[NiSiO_3]$ [47,48]. The joint use of XRD, ED, HRTEM and XPS results clearly shows that the following species are formed on the palygorskite surface: Nickel nanoparticles detectable by all these techniques, NiO

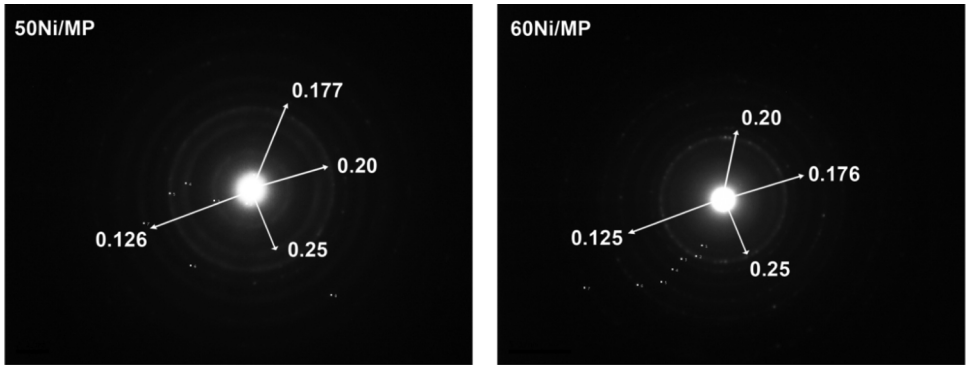

Fig. 1. Electron diffraction patterns for the samples 50Ni/MP and 60Ni/MP.

Table 2
Relative surface concentration of nickel appearing as metallic nickel (Ni^0), NiO and nickel silicates, determined by XPS.

Catalyst	Ni^0 (%)	NiO (%)	Nickel silicates (%)
10Ni/MP	0	13	87
20Ni/MP	41	21	38
30Ni/MP	32	33	35
40Ni/MP	46	25	29
50Ni/MP	31	42	27
60Ni/MP	41	37	24

nanocrystals smaller than 4 nm and thus non-detectable by XRD (JCPDS 22-1189) and surface nickel silicates ($NiSiO_3$ and/or $Ni_3Si_2O_5(OH)_4$), non-detectable by XRD (JCPDS 49-1859) and electron diffraction, detectable only by XPS.

Inspection of Figure S5 and Table 2 clearly shows that the relative percentage surface concentration of nickel participating in nickel silicates decreases drastically with the nickel content whereas that of metallic nickel plus nickel in nickel oxide increases. The zero % Ni value determined for the catalyst 10Ni/MP is in line with the XRD pattern recorded for this catalyst, which shows a very small peak at $2\theta = 44.38^\circ$, if any, and no peaks at 2θ equal to 51.72° and 76.17° assigned to metallic nickel.

Closing with the XPS results, it should be noted that the binding energies of $Fe2p_{3/2}$, Al2p and Mg2s, centered at 710.5 eV, 74.4 eV and 88.9 eV, were assigned, respectively, to Fe^{3+}, Al^{3+} and Mg^{2+} ions being in the support structure.

3.3. Morphology of the samples and size distribution of the supported Ni/NiO nanoparticles

The SEM investigation of the catalysts reveals a fibrous morphology for the support and a rather spherical morphology for the supported nanoparticles. An example is illustrated in Figure S6. The catalysts morphology was further investigated by TEM. The TEM images for all the samples are illustrated in Figure S7. Inspection of this figure confirms the fibrous morphology of palygorskite and the granular morphology of the supported nanoparticles deduced by SEM. Moreover, these pictures indicate that the size of the supported nanoparticles increases with the nickel content. Taking into account that the nickel silicate phases are not visible by XRD, ED and HRTEM, we are attributing the supported nanoparticles, illustrated in SEM and TEM images, to nickel/nickel oxide nanocrystals or nanoparticles comprised from these nanocrystals.

The increase of the size of the supported nickel/nickel oxide nanoparticles with the nickel content is presented quantitatively in the

Table 3
Mean size of the supported nickel nanocrystals determined by TEM and XRD.

Catalyst	Mean size / nm	
	TEM	XRD
0Ni/MP	–	–
10Ni/MP	5.26	6.3
20Ni/MP	6.02	6.5
30Ni/MP	6.79	6.5
40Ni/MP	7.67	6.5
50Ni/MP	10.14	9.0
60Ni/MP	12.40	11.2

particle size distributions illustrated in Fig. 3 for the catalysts with the minimum and maximum nickel content and in Figure S8 for all the catalysts studied. Inspection of these figures shows a progressive shift of the size distribution to higher values as the nickel content increases.

For example, in the sample with the minimum nickel content, the distribution is maximized in the range of sizes 4–6 nm, whereas the nanoparticles size does not exceed 10–12 nm. In contrast, in the sample with the maximum nickel content, the distribution is maximized in the range of sizes 8–12 nm, whereas a non-negligible population of supported nanoparticles is present even with sizes in the range 28–32 nm. The progressive shift of the distribution towards higher particle size brings about the increase of the *mean size* of the supported nanoparticles from 5.26 to 12.40 nm (Table 3 and Figure S8). A similar but not identical trend is observed for the mean crystal size of nickel nanoparticles determined by XRD. In this point it should be stressed that the shift of particle size distribution to higher values with the nickel content reflects the shift of size distribution of the *metallic nickel* supported nanoparticles, because the size of the nickel oxide nanocrystals does not exceed 4 nm (invisible in XRD).

3.4. Surface exposed by the nickel/nickel oxide supported nanoparticles

Taking into account the sizes of the nickel/nickel oxide supported nanoparticles determined by TEM images, we have calculated the nickel surface exposed both per gram of nickel and per gram of the catalyst as well. The results are presented in Table 4.

We are observing a continuous decrease of the nickel surface per gram of nickel. The effect is important as the S value decreases from 101 m^2/g Ni, for the catalyst with the minimum nickel loading, to 28 m^2/g Ni, for the catalyst with the maximum nickel loading. It is, however, much more practical using the nickel surface area per gram of catalyst, S*, because this parameter is more relevant to catalytic activity. We are observing that this parameter follows a like volcano trend: it increases up to the 40Ni/MP catalyst and then it decreases.

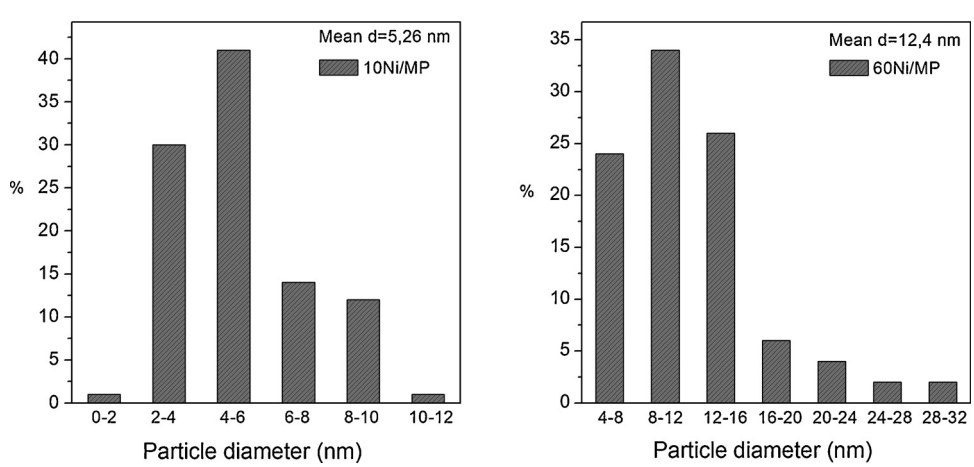

Fig. 3. Size distributions of the supported nickel/nickel oxide nanoparticles in the samples 10Ni/MP and 60Ni/MP.

Table 4
Nickel surface exposed in the catalysts studied.

Catalyst	S (m^2/g Ni)	S* (m^2/g catalyst)
10Ni/MP	101	10
20Ni/MP	94	19
30Ni/MP	81	24
40Ni/MP	63	26
50Ni/MP	47	24
60Ni/MP	28	18

However, the difference in the S* value between the 40Ni/MP and the 30Ni/MP sample is very small.

3.5. Texture of the support and location of nickel/nickel oxide supported nanoparticles

Table S1 compiles the values determined for several parameters of the texture of the catalysts studied. It is useful to mention that the S_{BET} values concern the surface area being inside the micropores (pore diameter up to 1.7 nm), the mesopores (pore diameter in the range 1.7–50 nm) and the macropores (pore diameter higher than 50 nm) as well as the external one. In contrast, the S_{MCR} and the S_{BJH} concern those in the micropores and in pores with diameter in the range of 1.7–100 nm, respectively. Inspection of Table S1 shows that the specific surface area of the support and the catalysts studied, S_{BET}, is mainly due to the mesoporous–macroporous in the range of 1.7–100 nm, S_{BJH}. A significantly smaller fraction of the surface is due to micropores, S_{MCR}, presumably developed between the triple layers of the palygorskite. Therefore, the samples studied are largely mesoporous. The increase in the nickel content causes a decrease in the S_{BET} and S_{BJH} values. However, these values, calculated per gram of support, remain practically constant up to the sample 20Ni/MP and then they increase. This presumably evidences a quite good dispersion of nickel supported nanoparticles inside the pores and thus no extended blockage of the pores. The increase in the S_{BET} and S_{BJH} values per gram of the support could be partly attributed to the surface added by the supported nickel/nickel oxide nanoparticles (Figures S6 and S7).

The shape of the pores was investigated by the adsorption–desorption isotherms (Figure S9). The shape of the isotherms and the hysteresis loops can be classified into the H3 or H4 types, indicating slit-shaped pores presumably developed between the fibrous of the solids presented in the SEM and TEM images (Figures S6 and S7).

The pore volume distribution curves of the catalysts provide a more detailed picture of the porous structure in the mesoporous range 2–50 nm (Figure S10). Although a dual distribution is emerged in all samples with the first peak centered at about 2.8–3.0 nm and the second at about 30 nm, the distribution curves indicate the presence of pores with various sizes in all mesoporous range. The presence of the small mesopores (2.8–3.0 nm) is certainly responsible for the high S_{BJH} values obtained. Moreover, the extrapolation of the curves at pores lower than 1.7 nm indicates that the pore volume values determined, though very small, are not negligible, confirming the micro-porosity mentioned before. The increase of the nickel content brings about a decrease in the pore volume for all pore sizes. As in the case of the S_{BET} and S_{BJH} values, this could partly reflect the decreasing amount of the porous support in the samples with the increase of the nickel content.

Let us now investigate the location of the nickel/nickel oxide nanoparticles on the porous support. The similar shape of the pore volume distribution curves (Figure S10) strongly suggests that these nanoparticles are located in all pores of the support, in agreement with the SEM and TEM results. There is no doubt that, as the size of the nickel nanoparticles increases with the nickel content (Figures S7 and S8), these are preferentially located to larger and larger pores. It should be reminded that the nickel oxide crystal size remains smaller than 4 nm. A first evidence for the location of the very small nickel/nickel oxide nanoparticles in the small mesopores provides the shift of the first peak of the pore volume distribution curves, from 3.0 to 2.8 nm, observed with the increase of the nickel content. The location of very small crystals *inside the micropores* can be inferred by the XRD patterns.

Concentrating our attention to the most intense peak of palygorskite (2θ = 7.98° (1 1 0), d = 1.10 nm, Fig. S2) which corresponds to the largest distance between the crystal planes (presumably developed between the triple layers of the palygorskite) we are observing significant shifts to both directions with increasing nickel content. The low angle XRD patterns (Figure S11) help us to investigate this point. The treatment of the palygorskite causes a shift of the 2θ value from 7.98 to 8.96° indicating a decrease in the distance between the crystalline levels (1 1 0), which is probably associated with the reduction of the diameter of the micropores. This can be associated to the heat treatment upon activation. The opposite effect is observed in the samples containing nickel. As the nickel content increases, the 2θ value is progressively decreases from 8.96° up to 7.33° in the sample 40Ni/MP and then it is slightly increases up to 7.93° in the sample 60Ni/MP. In order to explain this trend we are assuming that very small nickel/nickel oxide crystals and presumably the nickel silicates developed inside the micropores may pillar them increasing their size. The bigger nickel nanocrystals prevailing in the samples 50Ni/MP and 60Ni/MP cannot be inserted in the micropores and the pillared effect weakens.

3.6. Reducibility

The temperature programmed reduction profiles of the *precursor* catalysts are illustrated in Fig. 4.

The TPR curve obtained for the sample 0Ni/MP (not shown here) reveals that palygorskite is not reducible in the temperature range studied. Thus, the TPR peaks appeared in the nickel containing samples concern exclusively the supported nickel oxide nanoparticles and supported nickel silicates *both present in the precursor catalysts*. The TPR curve of the 10Ni/MP sample exhibits three peaks at about 520, 700 and 830 °C. Taking into account the XPS results, we are attributing the peak at 520 °C to the reduction of small NiO supported particles strongly interacted with the support surface and the peaks at 700 and 830 °C to the reduction of surface nickel silicates. In fact, these species, already present in the precursor state, do not undergone appreciable reduction up to 500 °C upon activation and thus they have been detected by XPS on the surface of the 10Ni/MP catalyst (Table 2, Figure S5). The increase of the nickel content brings about a dramatic decrease of the magnitude of the peaks at 700 and 830 °C, in line with the drastic decrease of the relative concentration of nickel silicates indicated by XPS (Table 2, Figure S5). However, the peak at 520 °C, assigned to relatively small NiO supported nanoparticles in the precursor state and

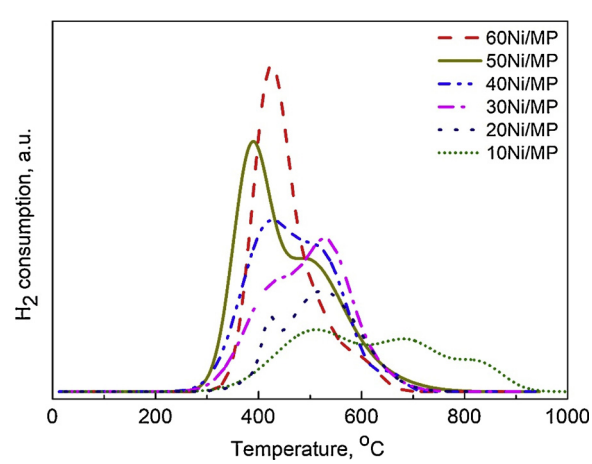

Fig. 4. Temperature programmed reduction profiles of the *precursor* catalysts studied.

thus strongly interacted with the support surface, becomes more intensive as the Ni loading increases up to 30% (30Ni/MP). This is in accordance with the XPS results, indicating that a significant fraction of Ni (21–33%) remains in the NiO state after activation at 500 °C (Table 2, Figure S5). A peak at about 420 °C appears, in addition, in the samples with nickel content higher than 10%. This peak can be effortlessly assigned to the reduction of larger nickel oxide nanoparticles weakly interacted with the support surface and thus easily reduced. The latter peak becomes predominant in the TPR profiles of the *precursor* catalysts with Ni loading ≥ 40 wt %, indicating that this kind of NiO nanoparticles is the main portion of the supported Ni in the corresponding *precursor* catalysts. This portion is totally reduced upon the activation at 500 °C leading to metallic nickel (XRD, ED, HRTEM and XPS results).

3.7. ζ-potential, surface charge and surface acidity

The title properties are interrelated and thus the relevant results are presented in the same subsection. Measuring the microelectrophoretic mobility of the samples in contact with an electrolytic solution and determining *ζ-potential* (the potential at shear plane of the interface developed between the surface of solid particles and the electrolytic solution [49]) is a suitable way for estimating the *surface charge* which is strongly related to the *Bronsted* surface acidity-basicity. The change of ζ-potential with pH is shown in Fig. 5. The isoelectric points determined from the ζ-potential vs pH curves are compiled in Table 5.

The values of equilibrium pH determined for the catalysts are also compiled in Table 5. These values are also related to the *Bronsted* surface acidity-basicity of the solid samples.

The surface acidity of the samples is also investigated by NH_3-TPD. The relevant curves are illustrated in Fig. 6.

Each of these curves was successfully deconvoluted into five curves with the exception of the sample 20Ni/MP where six curves are required for a successful description of the experimental NH_3-TPD curve. The deconvolution for each sample is illustrated in Figure S12. It has been generally accepted that the acid sites are classified into three types: weak (desorption temperature < 300 °C), intermediate (300 °C < desorption temperature < 450 °C), and strong (desorption temperature > 450 °C) [50,51]. Following the literature we have attributed the three NH_3-TPD peaks detected in the range 100–280 °C to week acid sites and the remaining peaks to intermediate acid sites. NH_3-TPD peaks at temperatures higher than 450 °C are not detected indicating the absence of strong acid sites.

The change of the population of the weak and moderately strong acid sites with the nickel content is illustrated in Fig. 7.

In order to interpret the results presented in this subsection it is necessary to recall the surface characteristics of the support and the catalysts, mostly deduced from the characterization presented. Concerning the support, we observe very small values of negative ζ-potential determined in the range of pH studied (Fig. 5) and a value for isoelectric point equal to 1.28 (Table 5). Moreover, the value obtained for the equilibrium pH is equal to 6.07 (Table 5). Finally, the NH_3-TPD study shows a quite high number of weak acid sites and very low population of intermediate acid sites (Fig. 7). These characteristics are quite similar to the corresponding ones determined for silica [52–55]. Moreover, these are compatible with the presence of the populated but too weak Si-OH acid sites of the palygorskite SiO_4 tetrahedral sheets and the less populated weak basic sites, Mg-OH, Fe-OH and Al-OH situated at the octahedral sheets of palygorskite. The contribution of

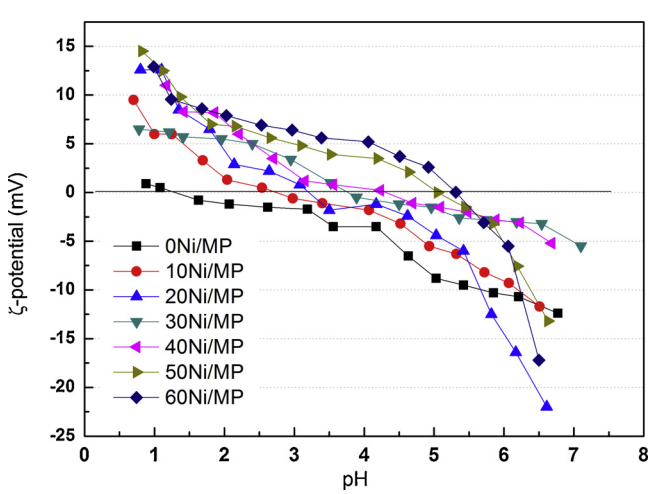

Fig. 5. Variation of the ζ-potential with pH for the catalysts studied.

Table 5
Values of the isoelectric point and equilibrium pH, determined for the catalysts studied.

Sample	Isoelectric point	Equilibrium pH
0Ni/MP	1.28	6.07
10Ni/MP	2.77	6.30
20Ni/MP	3.21	6.52
30Ni/MP	3.72	7.05
40Ni/MP	4.32	7.15
50Ni/MP	5.06	7.70
60Ni/MP	5.32	7.75

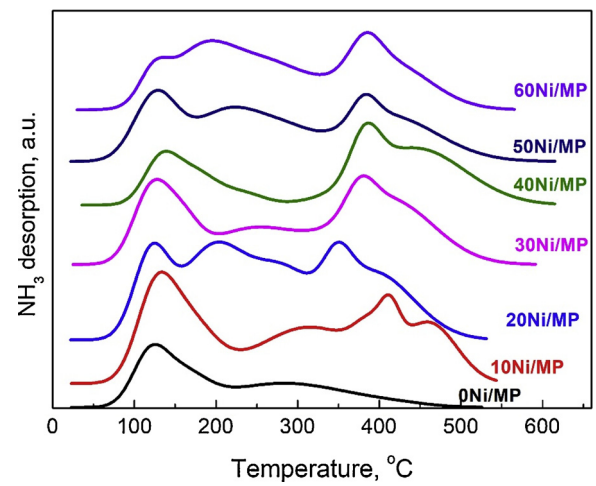

Fig. 6. NH_3-TPD curves determined for the samples studied.

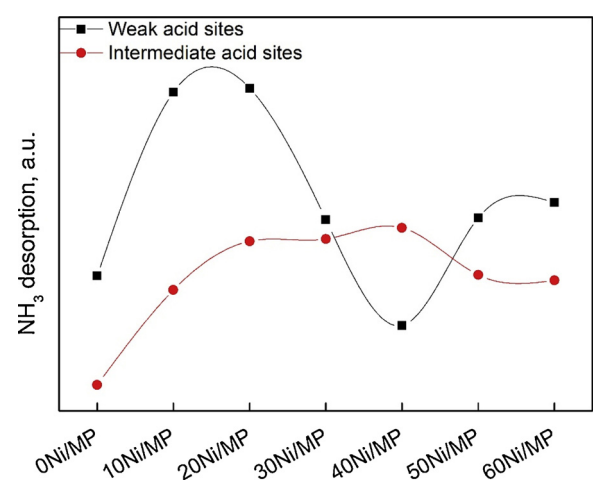

Fig. 7. Change of the population of the weak and intermediate acid sites with the nickel content.

these sites leads to a rather weak acidic surface from the view point of Bronsted acidity. The very small population of intermediate acid sites detected on the support (Fig. 7) can be attributed to the presence of small amounts of iron produced after activation (see Table 1).

The coverage of the support surface by the nickel/nickel oxide supported nanoparticles and nickel silicate species changes the surface acidity. The most important effect is the appearance of moderately strong acid sites, not practically present on the support (Fig. 7). It seems to us reasonable attributing this kind of sites to the formation of acid sites situated on the surface of the supported nickel phases. There are three reasons supporting this assignment: (a) The observation that these sites are present only on the surface of catalysts containing nickel. (b) The possibility of developing a surface bond through the interaction of the lone pair of electrons of ammonia with the empty *d* orbitals of the metallic nickel and the Ni^{2+} ions in the supported nickel oxide and nickel silicates. (c) The observation that the population of this kind of sites follows a trend with nickel content similar to that of the nickel surface exposed per gram of catalyst (Fig. 7, Table 4).

The coverage of the support surface by nickel phases changes also the surface acidity–basicity of the samples concerning the weak, rather Bronsted type, sites. The appearance of the weak basic sites is manifested by the positive values of ζ-potential at pH = 1, which imply the protonation of Me-OH surface groups and the development of positive surface charge. These can be due to the formation of NiO supported nanoparticles. On the surface of this oxide, of amphoteric type, both acid and basic, Bronsted, sites are indeed developed [56]. Taking into account that the isoelectric point of this oxide is close to 8.6 [56], one can easily understand the shift of the isoelectric point to higher values with nickel content (Table 5). The same is valid for the shift in the values of equilibrium pH. The trend of change of the weak, Bronsted, acidity with the nickel content is complicated (Fig. 7) indicating the influence of, at least, two opposite factors: the increase of this type of acidity due to the development of weak acid sites on the NiO supported nanoparticles [56] and the decrease of this type of acidity due to the coverage of the populated Si-OH weak acidic sites [52–55] by the nickel supported phases. However, the most important finding from the point of view of catalytic behavior is the development of moderately strong acid sites on the surface of the nickel containing catalysts.

3.8. Evaluation of the catalyst activity

The evaluation of the catalysts for transformation of WCO to green diesel via SDO process was carried out at 310 °C, hydrogen pressure 40 bar, reaction time up to 9 h and a ratio of volume of WCO to catalyst mass equal to 100 mL/1 g. Blank experiments taken place under these conditions showed that no reaction takes place in the absence of catalyst. In the presence of catalysts, besides the un-reacted WCO, the following molecules were detected in the liquid reaction mixture: n-heptadecane, n-octadecane, n-pentadecane, n-hexadecane, stearic acid, palmitic acid, stearic methyl ester, traces of n-octadecanol and big esters produced by esterification of the intermediate fatty acids and fatty alcohols. The n-alkanes produced are the end products constituting the *green diesel* whereas the remaining molecules are intermediate ones [6,9–11]. A representative chromatogram is depicted in Figure S13.

Fig. 8 illustrates the percentage conversion of the WCO as well as the percentage composition of the liquid reaction mixture in total n-alkanes, total acids and total big esters for reaction time equal to 9 h. As the percentage of octadecanol, stearic methyl ester and non-reacted WCO are negligible they are not presented in the figure. Inspection of Fig. 8 shows that a quite high conversion is obtained (51.9%) even over the surface of palygorskite (0Ni/MP), indicating that the support is quite active concerning the first few steps of SDO reaction mechanism [9,16,26–28] which involve the production of the intermediate acids (21.4% of liquid reaction mixture) and the big esters (27.4% of the liquid reaction mixture). The significant percentage of the big esters indicates that reduction of a fraction of the intermediate acids takes also place to the corresponding fatty alcohols. These react with the remaining fraction of acids to produce the big esters. In contrast, palygorskite is practically inactive concerning the steps of decarboxylation of acids, decarbonylation of the intermediate aldehydes and hydrodeoxygenation of the intermediate fatty alcohols to n-alkanes [9,16,26–28]. In fact, the percentage of n-alkanes in the liquid reaction mixture produced over palygorskite after 9 h of reaction did not exceeded 3.1 wt %.

The percentage conversion of WCO obtained over the catalysts containing nickel is 100% besides the catalyst with the maximum nickel content over which a value equal to 98.72% was achieved. Moreover, over the catalysts containing nickel, considerable amounts of n-alkanes were produced confirming once again that the supported nickel nanoparticles catalyze all the steps of SDO mechanism [9,16,26–28]. The percentage composition of the liquid reaction mixture in n-alkanes, the most important evaluation parameter from practical point of view, follows a volcano like trend. It increases with the nickel content (10Ni/MP (18.5%), 20Ni/MP (54.1%)) taking its maximum value in the catalyst 30Ni/MP (81.9%) and then it decreases (40Ni/MP (67.1%), 50Ni/MP (54.2%), 60Ni/MP (21.2%)). Taking into account the very high value of the volume of WCO to catalyst mass ratio (100 mL/1 g) and the solvent free conditions where the catalytic tests were performed, the percentage composition of the liquid reaction mixture in n-alkanes is very high [16]. This demonstrates that palygorskite is an excellent carrier for developing nickel supported catalysts to produce second generation green diesel. We attribute the excellent activity of the catalysts to the high dispersion ability of palygorskite in conjunction to the method followed for dispersing nickel on the support surface. These resulted to the formation of quite small supported nickel nanoparticles (Figures S7 and S8) and thus to quite large values of the nickel surface exposed (Table 4). It seems that the trend in catalytic performance concerning the produced n-alkanes follows somewhat similar trends to those of the nickel surface exposed and the intermediate acidity. Acidity plays an important role in several steps of the SDO reaction network [9,16,26–28]. Specifically, acid sites are involved in the C–O hydrogenolysis of the triglycerides resulting to intermediate fatty acids. Acid sites are also involved in the dehydration step of the intermediate fatty alcohols. Nevertheless, the strength of the acid sites is crucial for obtaining high catalytic performance. Very weak acid sites cannot accelerate sufficiently the aforementioned steps resulting to relatively low conversion of triglycerides. On the other hand, very strong acid sites could lead to no negligible fragmentation of the side chains of triglycerides resulting to low selectivity in hydrocarbons in the diesel range. Thus, moderate acidity is required for obtaining high catalytic performance. More information concerning the role of acidity in SDO of triglycerides has been reported in ref. [16]. In this point it should be noted that a portion of the NiO supported nanoparticles could be reduced to very small metallic nickel nanoparticles upon reaction taking place at very high hydrogen pressure (40 bar) and thus contributing to the creation of active sites, mainly located on metallic nickel [9,16,26–28]. This reduction has been demonstrated for SDO taking place under identical experimental conditions over similar catalysts by comparing XPS spectra recorded for fresh and spent catalysts [9].

The SDO kinetics performed over all samples studied confirmed that the first steps of the SDO network are actually rapid as it is inferred from the almost full percentage conversion values of WCO obtained after 2 h of reaction. A typical example is illustrated in Fig. 9.

Inspection of this figure shows, moreover, that while the composition of the liquid reaction mixture increases monotonically concerning the n-alkanes, this is not the case for the acids and the big esters confirming once again that these are intermediated molecules [9,16,26–28].

More understanding concerning the SDO mechanism followed in the present work can be obtained by determining the percentage composition of the liquid reaction mixture *in each one* of the hydrocarbons produced. The results obtained for various reaction times over the

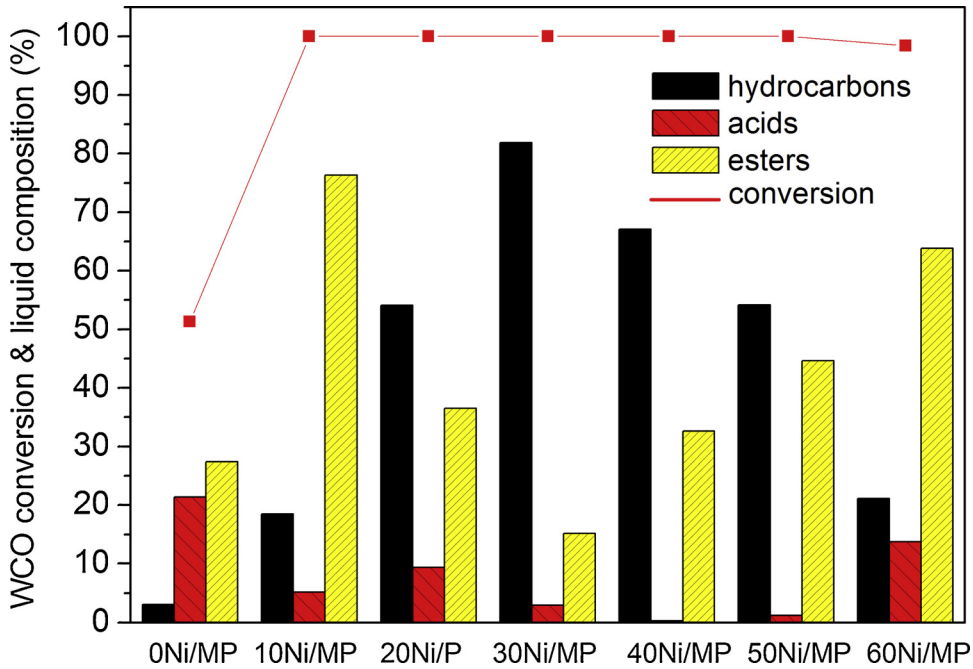

Fig. 8. The percentage conversion of the WCO and the percentage composition of the liquid reaction mixture in total hydrocarbons (n-alkanes), total acids and total big esters, obtained for reaction time equal to 9 h over the catalysts studied.

40Ni/MP catalyst are illustrated in Fig. 10.

The figure clearly shows that SDO over the catalysts results preferentially to n-alkanes with odd number of carbon atoms with respect to the corresponding ones with even number of carbon atoms. This demonstrates that the SDO mechanism in the present work proceeds mainly via the decarbonylation of the intermediate aldehyde instead of the dehydration of the intermediate alcohols. This behavior is typical of the nickel supported catalysts [16].

4. Conclusions

1 The deposition of various amounts of nickel on the surface of palygorskite via the deposition–precipitation technique does not actually disturb the chemical composition of the carrier as well as its crystal structure and fibrous morphology. Moreover, it does not affect its porous structure involving micropores and mainly mesopores with a dual pore size distribution centered at about 3 and 30 nm.

2 Nickel supported nanoparticles and very small NiO supported nanoparticles, both of rather spherical geometry, together with nickel

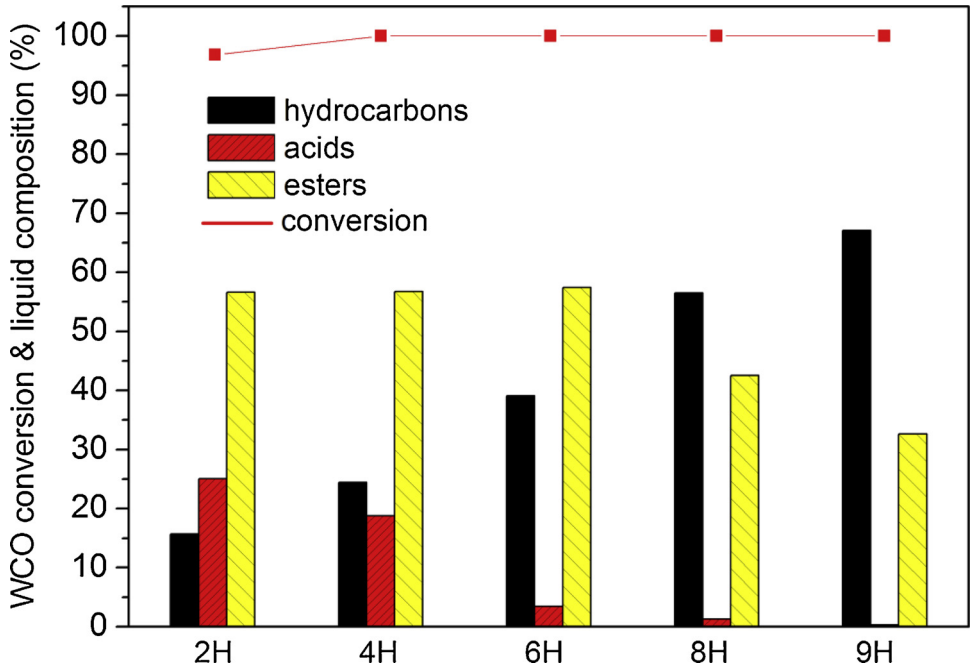

Fig. 9. The percentage conversion of the WCO and the percentage composition of the liquid reaction mixture in total n-alkanes, total acids and total big esters, obtained for various reaction times over the 40Ni/MP sample.

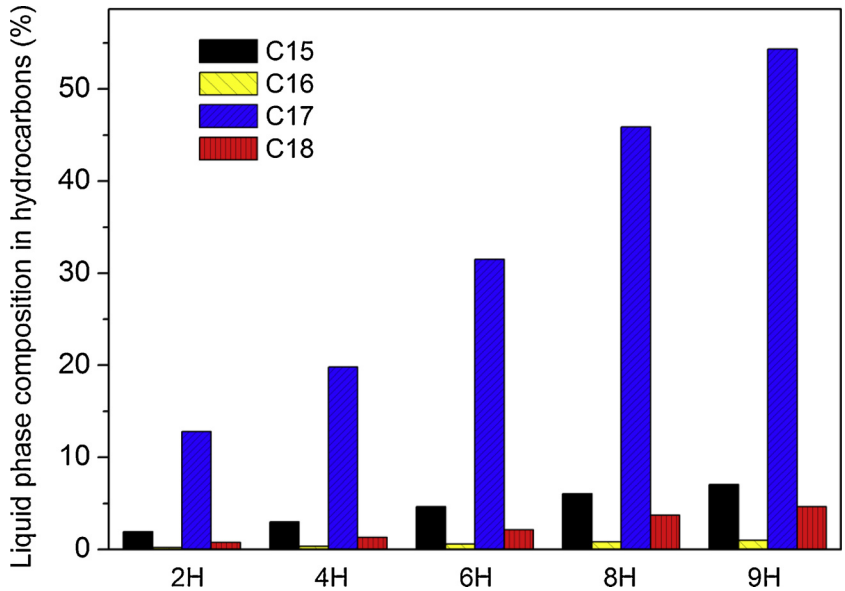

Fig. 10. The percentage composition of the liquid reaction mixture in each of the hydrocarbons obtained for various reaction times over the 40Ni/MP catalyst.

silicate species ($NiSiO_3$ and/or $Ni_3Si_2O_5(OH)_4$) are formed on the support surface. The latter are formed on the tetrahedral silicon layers of palygorskite and predominate in the catalyst with the minimum nickel content. As the nickel content increases the relative concentration of the nickel silicate species decreases. Moreover, larger and larger nickel nanocrystals are formed inside increasingly larger mesopores of palygorskite. This brings about a progressive decrease of the nickel surface exposed per gram of supported nickel and a like volcano trend for the nickel surface exposed per gram of catalyst. In the latter case, the maximum nickel surface is obtained in the 40Ni/MP catalyst. On the surface of the nickel phases moderately strong acid sites are developed.

3 The catalysts were evaluated under free solvent conditions and very high ratio of reactant volume to catalyst mass (100 mL/1 g) and were proved to be very active in the transformation WCO into green diesel, indicating that the mineral palygorskite is an excellent carrier for developing nickel supported catalysts to produce second generation green diesel. The conversion of WCO is of about 100% for all the catalysts studied, whereas the composition of the liquid reaction mixture in green diesel follows a volcano like trend, similar to that followed for the nickel surface exposed per gram of catalyst, which is maximized in the 30Ni/MP catalyst (81.9%). Kinetic experiments confirmed that the SDO network, well established over the nickel supported catalysts, is also valid for the nickel catalyst supported on palygorskite.

Declaration of Competing Interest

The authors declare that they have no known competing financial interests or personal relationships that could have appeared to influence the work reported in this paper.

Acknowledgment

We acknowledge support of this work by the project “AENAO-Materials and Processes for Energy and Environmental Applications” (MIS 5002556) which is implemented under the “Action for the Strategic Development on the Research and Technological Sector”, funded by the Operational Programme "Competitiveness, Entrepreneurship and Innovation" (NSRF 2014-2020) and co-financed by Greece and the European Union (European Regional Development Fund).

Appendix A. Supplementary data

Supplementary material related to this article can be found, in the online version, at doi:https://doi.org/10.1016/j.apcatb.2019.118059.

References

[1] J. Reilly, S. Paltsev, Biomass Energy and Competition for Land, MIT Joint Program on the Science and Policy of Global Change, (2007) Report #145 http://web.mit.edu/globalchange/www/MITJPSPGC_Rpt145.pdf (Accessed 9 October 2018).
[2] P.J. Crutzen, A.R. Mosier, K.A. Smith, W. Winiwarter, Atmos. Chem. Phys. 8 (2008) 389–398.
[3] F.H. Isikgor, C.R. Becer, Polym. Chem. 6 (2015) 4497–4559.
[4] D. Bolonio, M.-J. García-Martínez, M.F. Ortega, M. Lapuerta, J. Rodríguez-Fernandez, L. Canoira, Renew. Energy 132 (2019) 278–283.
[5] S. Liu, T. Simonetti, W. Zheng, B. Saha, ChemSusChem 11 (2018) 1446–1454.
[6] D. Singh, S.S. Sandhu, A.K. Sarma, Energy Sources Part A 40 (2018) 968–976.
[7] G.A. Alsultan, N. Asikin-Mijan, H.V. Lee, A.S. Albazzaz, Y.H. Taufiq-Yap, Energy Convers. Manage. 151 (2017) 311–323.
[8] G. Xu, Y. Zhang, Y. Fu, Q. Guo, ACS Catal. 7 (2017) 1158–1169.
[9] E. Kordouli, L. Sygellou, C. Kordulis, K. Bourikas, A. Lycourghiotis, Appl. Catal. B 209 (2017) 12–22.
[10] I. Hachemi, N. Kumar, P. Mäki-Arvela, J. Roine, M. Peurla, J. Hemming, J. Salonen, D.Yu. Murzin, J. Catal. 347 (2017) 205–221.
[11] R. Kaewmeesri, A. Srifa, V. Itthibenchapong, K. Faungnawakij, Energy Fuels 29 (2015) 833–840.
[12] K. Pongsiriyakul, W. Kiatkittipong, K. Kiatkittipong, N. Laosiripojana, K. Faungnawakij, S. Adhikari, S. Assabumrungrat, Energy Fuels 31 (2017) 12256–12262.
[13] A.F.H. Studentschnig, T. Telser, S. Schober, M. Mittelbach, Biofuels 7 (2016) 279–287.
[14] S. Phimsen, W. Kiatkittipong, H. Yamada, T. Tagawa, K. Kiatkittipong, N. Laosiripojana, S. Assabumrungrat, Energy Convers. Manage. 126 (2016) 1028–1036.
[15] I. Kubickova, D. Kubicka, Waste Biomass Valor. 1 (2010) 293–308.
[16] C. Kordulis, K. Bourikas, M. Gousi, E. Kordouli, A. Lycourghiotis, Appl. Catal. B 181 (2016) 156–196.
[17] C. Zhao, T. Brück, J.A. Lercher, Green Chem. 15 (2013) 1720–1739.
[18] R.W. Gosselink, S.A.W. Hollak, S.-W. Chang, J. van Haveren, K.P. de Jong, J.H. Bitter, D.S. van Es, Chem. Sus. Chem. 6 (2013) 1576–1594.
[19] K.B. Baharudin, Y.H. Taufiq-Yap, J. Hunns, M. Isaacs, K. Wilson, D. Derawi, Microporous Mesoporous Mater. 276 (2019) 13–22.
[20] S. Zulkepli, J.C. Juan, H.V. Lee, N.S.A. Rahman, P.L. Show, E.P. Ng, Energy Convers. Manage. 165 (2018) 495–508.
[21] I. Hachemi, N. Kumar, P. Mäki-Arvela, J. Roine, M. Peurla, J. Hemming, J. Salonen, D.Yu. Murzin, J. Catal. 347 (2017) 205–221.
[22] C.V. Viêgas, I. Hachemi, S.P. Freitas, P. Mäki-Arvela, A. Aho, J. Hemming, A. Smeds, I. Heinmaa, F.B. Fontes, D.C. da Silva Pereira, N. Kumar, D.A.G. Aranda, D.Yu. Murzin, Fuel 155 (2015) 144–154.
[23] J.-O. Shim, K.-W. Jeon, W.-J. Jang, H.-S. Na, J.-W. Cho, H.-M. Kim, Y.-L. Lee, D.-W. Jeong, H.-S. Roh, Ch.H. Ko, Appl. Catal. B 239 (2018) 644–653.
[24] T.N. Kalnes, K.P. Koers, T. Marker, D.R. Shonnard, Sustain. Energy 28 (2009) 111–120.

[25] S. Chen, G. Zhou, H. Xie, Z. Jiao, X. Zhang, Appl. Catal. A Gen. 569 (2019) 35–44.
[26] M. Gousi, C. Andriopoulou, K. Bourikas, S. Ladas, M. Sotiriou, C. Kordulis, A. Lycourghiotis, Appl. Catal. A Gen. 536 (2017) 45–56.
[27] E. Kordouli, PhD Thesis (2017) Department of Chemistry, University of Patras (Greece).
[28] E. Kordouli, B. Pawelec, K. Bourikas, C. Kordulis, J.L.G. Fierro, A. Lycourghiotis, Appl. Catal. B: Environ. 229 (2018) 139–154.
[29] H. Liu, T. Chen, X. Zhang, J. Li, D. Chang, L. Song, Chin. J. Catal. 31 (2010) 409–414.
[30] H. Liu, T. Chen, D. Chang, D. Chen, H. He, R.L. Frost, J. Mol. Catal. A Chem. 363–364 (2012) 304–310.
[31] N. Laosiripojana, W. Sutthisripok, S. Charojrochkul, S. Assabumrungrat, Fuel Proc. Technol. 127 (2014) 26–32.
[32] H. Liu, T. Chen, D. Chang, D. Chen, H. He, P. Yuan, J. Xie, R.L. Frost, Appl. Clay Sci. 74 (2013) 135–140.
[33] T. Chen, H. Liu, P. Shi, D. Chen, L. Song, H. He, R.L. Frost, Fuel 107 (2013) 699–705.
[34] Y. Wang, M. Chen, Z. Yang, T. Liang, S. Liu, Z. Zhou, X. Li, Appl. Catal. A Gen. 550 (2018) 214–217.
[35] D. Makarouni, S. Lycourghiotis, E. Kordouli, K. Bourikas, C. Kordulis, V. Dourtoglou, Appl. Catal. B 224 (2018) 740–750.
[36] S. Lycourghiotis, D. Makarouni, E. Kordouli, K. Bourikas, C. Kordulis, V. Dourtoglou, Mol. Catal. 450 (2018) 95–103.
[37] T. Holtzapffel, Les minéraux argileux: préparation, analyse diffractométrique et détermination. Société Géologique du Nord, Publication No. 12, Villeneuve d' ASCQ, France, 1985, p. 136.
[38] A. Liberman, Analyst 80 (1955) 595–598.
[39] F. Gonjalez, C. Pesquera, C. Blanco, I. Benito, S. Mendioroz, J.A. Pajares, Appl. Clay Sci. (1989) 373–388.
[40] M. Suarez Barrios, L.V. Flores Gonzalez, M.A. Vicent Rodriguez, J.M. Martin Pozas, Appl. Clay Sci. 10 (1995) 247–258.
[41] M. Myriam, M. Suarez, J.M. Martin-Rozas, Clays Clay Miner. 46 (1998) 225–231.
[42] Y. Liu, W. Dai, T. Wang, Y. Tao, J. Cent. South Univ. Technol. 13 (4) 451-455.
[43] N. Frini-Srasra, E. Srasra, Desalination 250 (2010) 26–34.
[44] R.N. Oliveira, W. Acchar, G.D.A. Soares, L.S. Barreto, Mater. Res. 16 (4) (2013) 924–928.
[45] A.P. Grosvenor, M.C. Biesinger, R.S. Smart, N.S. McIntyre, Surf. Sci. 600 (2006) 1771–1779.
[46] Y. Zhang, W. Zhou, H. Yu, T. Feng, Y. Pu, H. Liu, W. Xiao, L. Tian, Nanoscale Res. Lett. 12 (2017) 325.
[47] A.R. Gonzhlez-Elipe, R. Alvarez, J.P. Holgado, J.P. Espinos, G. Munuera, Appl. Surf. Sci. 51 (1991) 19–26.
[48] Z.-Q. Liu, X.-Y. Wei, X. Zhou, Y.-C. Xiao, Z.-K. Li, X.-H. Guo, S.-K. Wang, Y.-Y. Zhang, Z.-M. Zong, F.-Y. Ma, J.-M. Liu, Fuel Proc. Technol. 161 (2017) 85–94.
[49] G.D. Panagiotou, T. Petsi, K. Bourikas, C.S. Garoufalis, A. Tsevis, N. Spanos, C. Kordulis, A. Lycourghiotis, Adv. Colloid Interface Sci. 142 (2008) 20–42.
[50] J. Grzechowiak, J. Rynkowski, I. Wereszczako-Zielinska, Catal. Today 65 (2001) 225–231.
[51] D. Zhang, W.-Q. Liu, Y.-A. Liu, U.J. Etim, X.-M. Liu, Z.-F. Yan, Chem. Eng. J. 330 (2017) 706–717.
[52] M. Pfeiffer-Laplaud, D. Costa, F. Tielens, M.-P. Gaigeot, M. Sulpizi, J. Phys. Chem. C 119 (2015) 27354–27362.
[53] M. Kosmulski, Adv. Colloid Interface Sci. 251 (2018) 115–138.
[54] M. Sulpizi, M.-P. Gaigeot, M. Sprik, J. Chem. Theory Comput. 8 (2012) 1037–1047.
[55] A.H. Jalil, U. Pyell, J. Phys. Chem. C 122 (2018) 4437–4453.
[56] T. Mahmood, M.T. Saddique, A. Naeem, P. Westerhoff, S. Mustafa, A. Alum, Ind. Eng. Chem. Res. 50 (2011) 10017–10023.